Schweizerische Eidgenossenschaft
Confédération suisse
Confederazione Svizzera
Confederaziun svizra

Federal Department of the Environment, Transport, Energy and Communications DETEC

Swiss Federal Office of Energy SFOE
Energy Research and Cleantech

Final report

CIGSPSC

Highly efficient perovskite solar cells for tandem devices fabricated by industrially relevant and scalable deposition methods

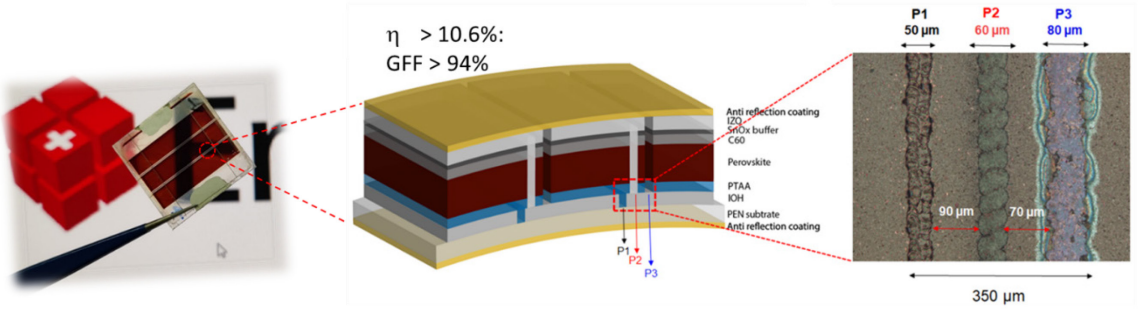

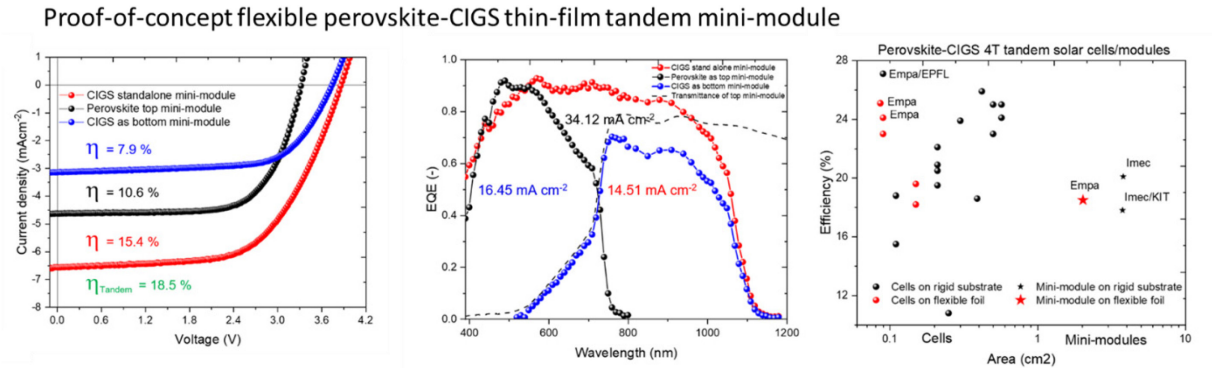

Source: ©Empa 2022

Date: 23.03.2022

Location: Dübendorf

Publisher:
Swiss Federal Office of Energy SFOE
Energy Research and Cleantech
CH-3003 Bern
www.bfe.admin.ch

Subsidy recipients:
Empa
Laboratory for Thin Films and Photovoltaics
Überlandstrasse 129
8600 Dübendorf
www.empa.ch

Authors:
Radha Kothandaraman, radha.kothandaraman@empa.ch
Severin Siegrist, severin.siegrist@empa.ch
Thierry Moser, thierry.moser@empa.ch
Fan Fu, fan.fu@empa.ch
Ayodhya N. Tiwari, ayodhya.tiwari@empa.ch

SFOE project coordinators:
SFOE head of domain: Stefan Oberholzer, stefan.oberholzer@bfe.admin.ch
SFOE programme manager: Stefan Oberholzer, stefan.oberholzer@bfe.admin.ch
SFOE contract number: SI/501805-01

Zusammenfassung

Halogenid-Perowskit-Solarzellen (PSCs) haben in den letzten zehn Jahren enorme Fortschritte gemacht und erreichen heute einen zertifizierten Wirkungsgrad von über 25 %. Die Skalierbarkeit von hocheffizienten Perowskit-Solarzellen ist eine der größten Herausforderungen bei der Herstellung von Solarmodulen. Es wurden verschiedene skalierbare Methoden erforscht, um einheitliche Perowskit-Filme von hoher Kristallqualität auf großflächigen Substraten zu erzeugen, aber jede dieser Methoden hat individuelle Beschränkungen für das Potenzial einer erfolgreichen Kommerzialisierung der Perowskit-Photovoltaik. Das Ziel dieses Projekts war die Entwicklung effizienter und stabiler flexibler NIR-transparenter Perowskit-Solarzellen und -Minimodulen für Tandemanwendungen. Für die Perowskit-Absorber, die Ladungstransportschichten und die transparenten Elektroden wurden ausschließlich industrie-relevante und in Fläche und Abscheidegeschwindigkeit skalierbare Abscheidungsmethoden eingesetzt. Darüber hinaus untersuchten wir die Leistungsstabilität von NIR-transparenten Perowskit-Solarzellen unter Betriebsbedingungen und klärten den mikroskopischen Degradationsmechanismus auf. Schließlich entwickelten wir eine vollständig lasergestützte Zellverschaltung für flexible NIR-transparente Perowskit-Minimodule und demonstrierten die ersten flexiblen Perowskit-CIGS-Tandem-Minimodule mit einem Wirkungsgrad von über 16 %.

Summary

Halide perovskite solar cells (PSCs) have shown tremendous advancements in the past ten years, now reaching certified power conversion efficiency (PCE) over 25%. The scalability of highly efficient perovskite solar cells is one of the major challenges of solar module manufacturing. Various scalable methods have been explored to strive for uniform perovskite films of high crystal quality on large-area substrates, but each of these methods has individual limitations on the potential of successful commercialization of perovskite photovoltaics. The aim of this project was to develop efficient and stable flexible NIR-transparent perovskite solar cells and mini-modules for tandem application. We employed only deposition methods that are industrially relevant and scalable in area and deposition speed for perovskite absorbers, charge-transport layers, and transparent electrodes. In addition, we investigated the performance stability of NIR-transparent perovskite solar cells under operating conditions and elucidate the microscopic degradation mechanism. Finally, we developed all-laser scribing cell interconnection for flexible NIR-transparent perovskite mini-module and demonstrate the first flexible perovskite-CIGS tandem mini-modules with over 16% efficiency.

Résumé

Les cellules solaires à pérovskite (PSC) à base d'halogénure ont fait d'énormes progrès au cours des dix dernières années, atteignant désormais un rendement de conversion de puissance (PCE) certifié supérieur à 25 %. La mise à l'échelle de cellules solaires à pérovskite hautement efficaces est l'un des principaux défis de la fabrication de modules solaires. Diverses méthodes de mise à l'échelle ont été explorées pour tenter d'obtenir des films de pérovskite uniformes de haute qualité cristalline sur des substrats de grande surface, mais chacune de ces méthodes présente des limites individuelles sur le potentiel de commercialisation réussie des cellules photovoltaïques en pérovskite. L'objectif de ce projet était de développer des cellules solaires et des mini-modules de pérovskite flexibles, efficaces et stables, transparents dans le proche infrarouge, pour une application en tandem. Nous avons utilisé uniquement des méthodes de dépôt qui sont pertinentes pour l'industrie et évolutives en termes de surface et de vitesse de dépôt pour les absorbeurs de pérovskite, les couches de transport de charge et les électrodes transparentes. En outre, nous avons étudié la stabilité des performances des cellules solaires en pérovskite transparentes dans le proche infrarouge dans des conditions d'exploitation et

élucidé le mécanisme de dégradation microscopique. Enfin, nous avons développé une interconnexion de cellules par gravure au laser pour des mini-modules flexibles en pérovskite transparente dans le proche infrarouge et démontré les premiers mini-modules tandem pérovskite-CIGS flexibles avec une efficacité de plus de 16 %.

Main findings

Our main findings are summarized as follows:

1. We successfully developed processes for growth of perovskite absorber layers. In the first approach metal halide template layer grown by physical vapor deposition (PVD) was subsequently reacted by chemical vapor deposition (CVD) of oregano-halide. A novel CVD reactor design with separate heating zones for substrate and source, and a switchable carrier gas flow were employed to attain a fine control over the perovskite processing conditions of temperature and time. This novel reactor design allows carrying out a systematic study to understand the reaction kinetics of perovskite formation using the CVD process under various processing conditions. Despite the promising results, we encountered enormous reproducibility issues with a method using an in-house developed CVD reactor and suggest a specifically customized design for the specific purpose.

2. We developed a novel and scalable PVD-Blade coating method, which combines potential advantages of vapor- and solution-based techniques to deposit high-quality uniform perovskite films on large-area substrates. This method allows depositing high-quality perovskite absorbers using a non-toxic solvent in ambient air. Together with blade coated electron and hole transport layers, we demonstrate over 18% perovskite solar cells with good uniformity on 5 cm × 5 cm substrates where all the layers are deposited using industrial scalable methods.

3. We revealed an I_2 vapor-assisted self-propagating degradation mechanism in NIR-transparent perovskite solar cells stressed under operational conditions at 80 °C under an N_2 atmosphere. At high operational temperature, the degradation initiates primarily from the perovskite absorber interior instead of the perovskite/charge-selective layer interfaces or cell edges. After an initial release either from traces of PbI_2 or from the perovskite itself, I_2 deteriorates the neighboring perovskite, releasing more I_2 to continue self-inflicted degradation, which propagates across the active area. We show that the degradation pattern is independent of the perovskite composition and preparation method, charge selective layers, and top transparent contact, suggesting the universality of this I_2 vapor-assisted degradation mechanism in iodide containing halide perovskites. Overall, our results present new insights into the degradation mechanisms of perovskite solar cells operating under long-term light soaking conditions at high temperatures.

4. We developed an all-laser scribing procedure for cell interconnection on the flexible substrates with geometrical fill factor (GFF) over 94% for mini-modules. Using all-laser scribed cell interconnection, we demonstrate the first flexible NIR-transparent perovskite mini-module with an efficiency of 10.6%. Together with a flexible CIGS mini-module, we demonstrated a proof-of-concept perovskite-CIGS flexible tandem mini-module with 18.5%.

Contents

Abbreviations

SFOE	Swiss Federal Office of Energy
CIGS	$Cu(In,Ga)Se_2$
PSC	Perovskite solar cell
TRL	Technology readiness level
ALD	Atomic layer deposition
PVD	Physical vapour deposition
CVD	Chemical vapour deposition
MFC	Mass flow controller
HTL	Hole transport layer
ETL	Electron transport layer
CTL	Charge transport layer
NIR	Near infrared
XRD	X-ray diffraction
XRF	X-ray fluorescence
SLG	Soda lime glass
PCE	Power conversion efficiency
JV	Current-Voltage
V_{oc}	Open circuit voltage
J_{sc}	Short circuit current
MPP	Maximum power point
EQE	External quantum efficiency
GFF	Geometrical fill factor
ITO	Tin doped indium oxide
IO:H	Hydrogen doped indium oxide
SEM	Scanning electron microscope

1 Introduction

1.1 Background and motivation

The rapid rise of perovskite solar cell efficiencies has been governed by improvements in the absorber deposition methodologies. The most efficient PSC displays an efficiency of > 25% realized on rather small area (~0.1 cm^2).[1] This device is grown on glass/FTO commercial substrates (FTO has strong parasitic absorption in the NIR-range, hence not ideal for tandem applications). The electron transport layer consists of a compact layer of TiO_2 deposited by spray pyrolysis, covered with a mesoporous TiO_2 film by spin coating (calcined at 500 °C, not suitable for transparent flexible substrates). The absorber $(FAPbI_3)_{0.95}(MAPbBr_3)_{0.05}$ is deposited by one-step spin coating in DMF/DMSO mixed solvent, with anti-solvent step just before annealing. The device is then completed with a Spiro-OMeTAD hole transport layer by spin coating and gold back contact by thermal evaporation.

Spin coating methods are not suitable for large-area processing required for industrial production. Alternative options for uniform large area coating could be printing or spraying of inks or solutions [2-3], or vacuum based chemical or physical vapor deposition [4-5]. Each of these methods have pros and cons, and require critical investigation to prove the potential.

There are numerous challenges for printing/spray deposition including different wettability of each layer in the full device stack, which could give rise to detrimental inhomogeneities during continuous deposition.[6] For industry relevant process, also the cost of ownership and the operation costs have to be considered. The use of hazardous solvents, the thorough cleaning of waste liquid and the protection of the stack form humidity and dust during processing must be taken into account for full cost analysis when dealing with printing or spraying processes. On the other hand, vacuum-based deposition approaches enable homogeneous material deposition over large areas, avoiding any challenge related to solution flow dynamics, wettability or exposure to moisture and oxygen. Moreover, the vacuum-based deposition method has been successfully employed in commercially available thin film solar cells including CIGS and CdTe. In this project, we explore the feasibility of preparing high-quality perovskite solar cells and mini-modules using industrially relevant and scalable deposition methods.

1.2 Objectives

Measurable targets and results to be reached within the project are:

1. Near-infrared region (NIR) transparent perovskite top cell fabricated by industrially relevant, scalable deposition methods on flexible substrate with energy bandgap optimized for tandem application yielding efficiency above 18% and NIR transmittance above 75% (800-1200 nm).

2. Interconnection concept that facilitates NIR transparent perovskite mini-modules (>10cm^2) on flexible substrate with efficiency above 15% and NIR transmittance above 75% (800-1200 nm).

3. Performance stability and intrinsic degradation mechanisms investigation.

4. Demonstration of 4-terminal tandem mini-module (both devices measured simultaneously) and evaluation of the potential.

2 Procedures and methodology

To achieve the abovementioned objectives, four work packages (WP) containing different tasks were planned.

In WP1, NIR-Transparent perovskite solar cells were developed. This WP consist the following tasks: Task 1.1: Design and setup of PVD, CVD and remote plasma sputtering equipment. Task 1.2: Perovskite absorber layers by scalable methods with optimized band gap. Task 1.3: Inorganic ETL/HTL and TCO layers. Task 1.4: NIR transparent top cell with efficiency above 18%.

In WP2, NIR-transparent perovskite mini-module were developed using the perovskite, charge transport layers and TCO developed in WP1. In addition, laser scribing recipes were developed for cell interconnection on the flexible substrates. To achieve high module efficiencies, a selective and complete removal of specific layers was performed for each scribing lines, i.e., P1, P2 and P3. Laser wavelength, pulse durations and powers were assessed to achieve optimal interconnections. Positions of each scribing lines were evaluated to minimize dead area and electrical shunts.

In WP3, perovskite solar cells were subjected to accelerated stress tests to gain insights on the microscopic degradation mechanism. Perovskite solar cells processed by the scalable deposition methods were continuous illuminated under irradiation equivalent to 1 sun at the maximum power point (MPP) tracking condition at elevated temperature (up to 80 °C). Macroscopic degradation pathways and microscopic degradation mechanism of eventual catastrophic failures will be analyzed.

In WP4, NIR-transparent perovskite mini-modules were integrated with CIGS bottom mini-modules (deposition process developed by Empa) as 4 terminal tandem mini-module.

3 Results and discussion

3.1 WP1 – NIR transparent top cell development

3.1.1 Design and setup of PVD and CVD systems

To achieve perovskite absorber with a fully scalable deposition process, we adopted a fully vacuum-based PVD-CVD deposition route, where a thermally evaporated inorganic halide precursor template was converted into perovskite absorber by reacting with sublimed organic halide vapor. A novel CVD reactor design (**Figure 1a** and **b**) with separate heating zones for substrate and source, and a switchable carrier gas flow were employed to attain a fine-control over the perovskite processing window (**Figure 1c**). The novel reactor design allows carrying out a systematic study to understand the reaction kinetics of perovskite formation using the CVD process under various processing conditions. The phase evolution of perovskite under different sublimation and source temperature, and with varying reaction time were studied and a processing window to obtain completely converted perovskite layers was established. Further, insights about under- and over-conversion region and decomposition regime were also identified (**Figure 1d**).

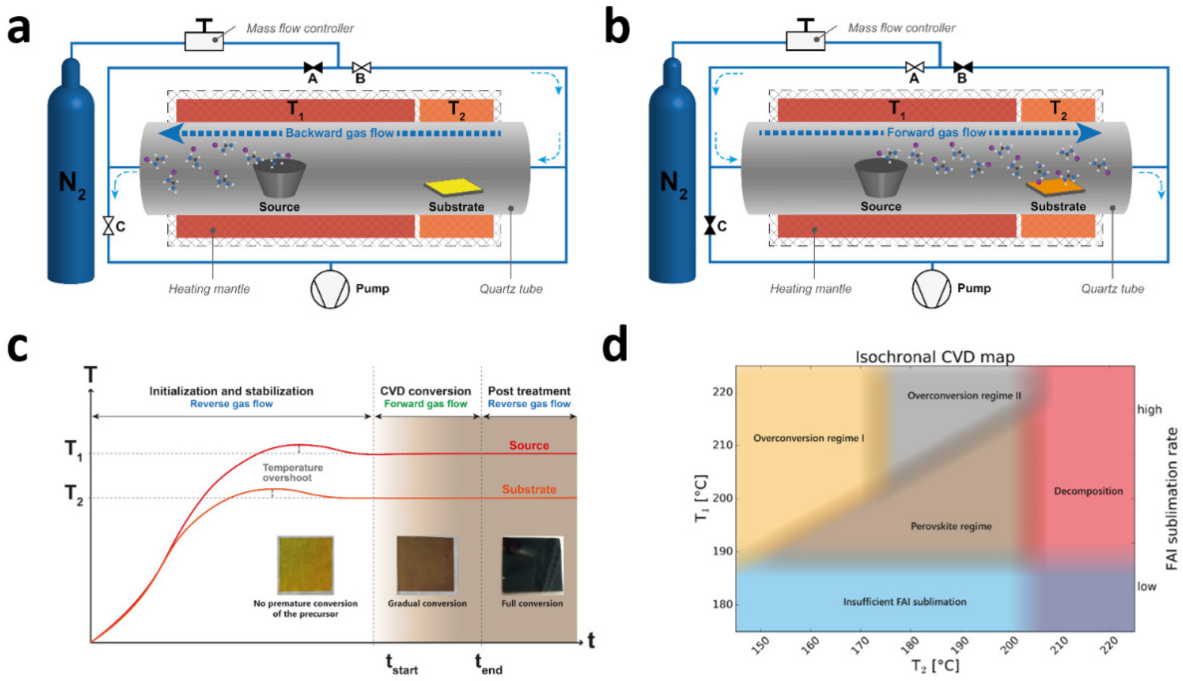

Figure 1. Perovskite formation using PVD-CVD process. **a** and **b** Schematic of the CVD reactor, allowing quick reversal of carrier gas flow. Depending on the flow direction, the premature reaction process is prevented before attaining the stabilized thermal conditions. **c,** Time–temperature-dependent reaction graph with control of carrier gas flow direction. **d,** Schematic of the isochronal CVD processing map showing five different regimes.

3.1.2 **Perovskite absorber layers by scalable methods**

To show the scalability of the PVD-CVD approach, perovskite layer was deposited on a 5 cm x 5 cm fused silica substrate (**Figure 2a**). The XRD patterns (**Figure 2b**) of 9 different spots on the sample show a full conversion, i.e., no precursor material was detected anymore. To further characterize the uniformity, the UV-Vis spectroscopy was utilized to obtain the optical depth (thickness) of the perovskite layer in 9 different areas (**Figure 2c**). The measurements show that the perovskite layer is thickest in the middle and thinner in the edge/corner areas. A thickness difference of less than 10% was obtained. However, non-uniform perovskite layers resulting from under- or over- conversion of the PVD grown precursor layer by CVD were also observed. Hence, detailed investigation of the CVD conversion kinetics was performed to investigate the dependencies on processing parameters used in CVD reactor [7]. To characterize the photovoltiac performance of the absorber grown by PVD-CVD, near-infrared (NIR) transparent perovskite cells were fabricated with the device architecture shown in **Figure 2d**. The charge selective layers (PTAA, PCBM, and ZnO nanoparticles) are spin coated, and the AZO layer is deposited with a multi-step RF-magnetron sputtering process to reduce sputtering damage. The NIR-transparent solar cell reached power conversion efficiency of 12.4% in backward J-V scan (**Figure 2e**) and a stabilized power output of >10.8% under MPP-tracking (**Figure 2f**).

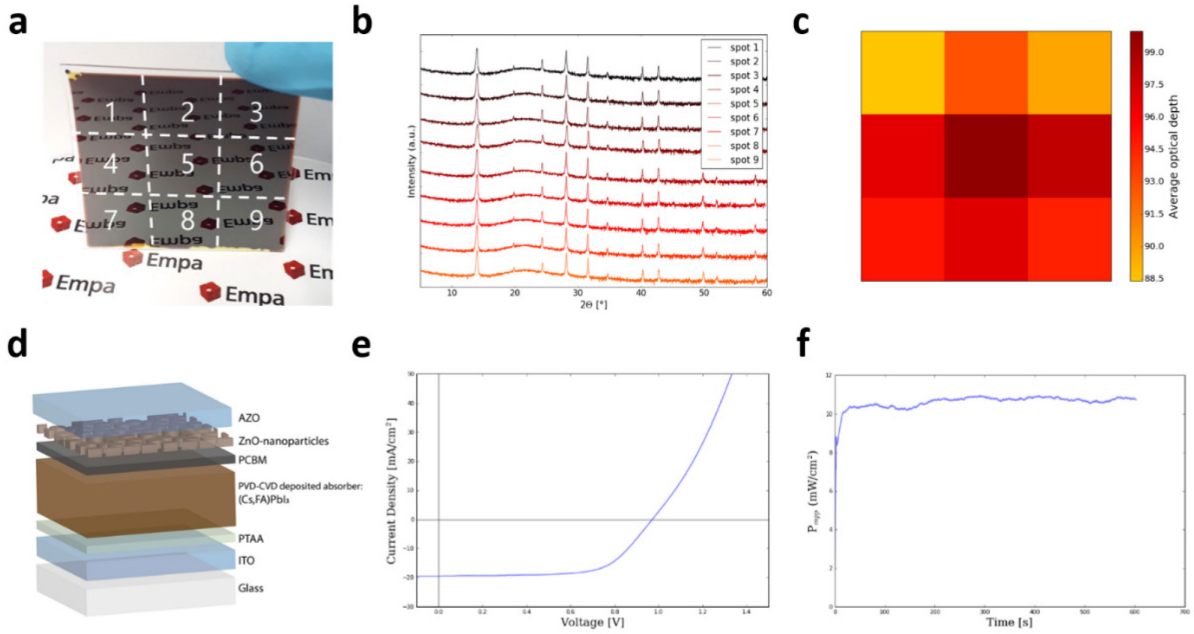

Figure 2. **a**, Photograph of the perovskite layer with the 9 probing areas indicated. **b**, XRD patterns of the 9 different areas, showing a single-phase perovskite layer. **c**, Optical depth map of the perovskite layer. **d**, Schematic device structure of NIR-transparent perovskite solar cell. **e**, **f**, J-V curve (**e**) and MPP tracking (**f**) of the best cell.

3.1.3 **NIR-transparent perovskite top cell with targeted efficiency above 18%**

Due to the challenges and difficulties encountered for PVD-CVD process as detailed later, efficient NIR-transparent perovskite top cell could not be realized on flexible substrate. The development of NIR-transparent PSCs on CIGS encapsulation sheet opens up a great possibility to integrate the perovskite top cell into CIGS production line to attain flexible 4-terminal tandem module with minimal additional cost as shown in **Figure 3**. With close collaboration with Flisom**,** Empa developed NIR-transparent perovskite solar cells directly on CIGS encapsulation foil. As a proof of concept, flexible NIR-transparent PSCs prepared with spin coating perovskite absorber yields steady state efficiency of 17.5%. Combing with 20% flexible CIGS cell, we demonstrate over 24% flexible perovskite-CIGS 4-terminal tandem cells. These are the highest values for both flexible NIR-transparent perovskite solar cells and flexible perovskite-CIGS tandem solar cells. The absolute efficiency gain in tandem cell is around 4% compare to the highest single junction cell. Future work will be focus on developing highly efficient NIR-transparent perovskite solar cells and modules with all layers deposited by scalable methods.

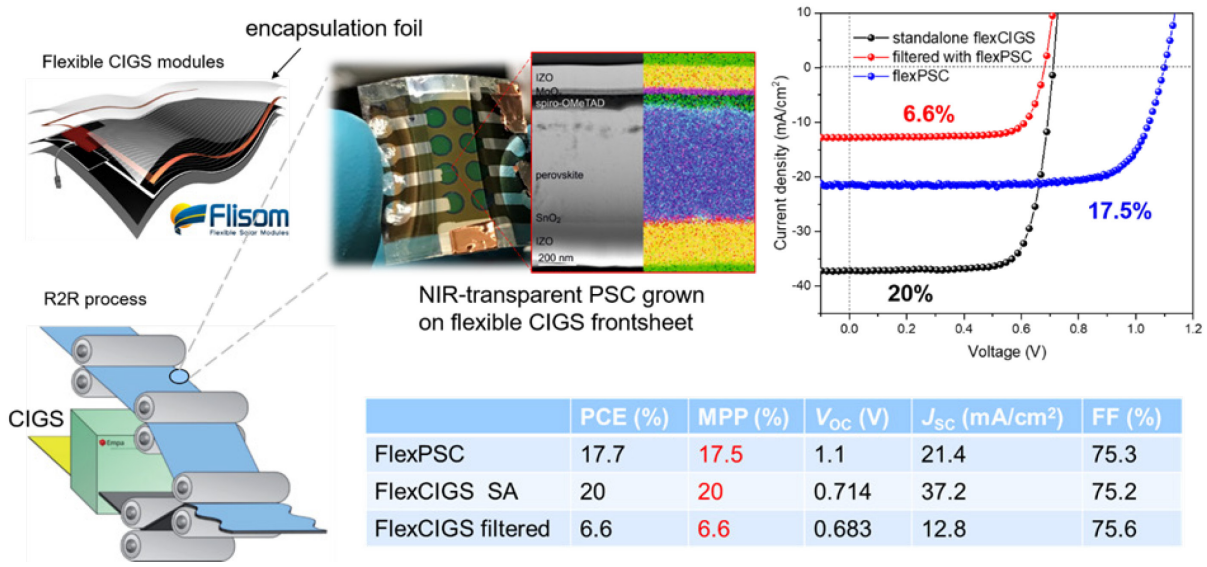

	PCE (%)	MPP (%)	V_{OC} (V)	J_{SC} (mA/cm²)	FF (%)
FlexPSC	17.7	17.5	1.1	21.4	75.3
FlexCIGS SA	20	20	0.714	37.2	75.2
FlexCIGS filtered	6.6	6.6	0.683	12.8	75.6

Figure 3. Schematic of a futuristic roll-to-roll manufacturing of mechanically stacked 4-terminal perovskite-CIGS flexible tandems. The perovskite cells are directly grown on flexible polymer that is used to encapsulate CIGS. Combining 17.5% flexible NIR-transparent perovskite top cell and 20% flexible CIGS bottom cell, we demonstrate over 24% flexible perovskite-CIGS tandem cell in 4-terminal configuration.

3.1.4 Challenges and difficulties

Although promising results (**Figure 2**) were achieved with PVD-CVD processed perovskite absorber, strong reproducibility issues were encountered. However, after the initial trails, a strong reduction in the conversion rate (**Figure 4a**) and very low solar cell performance were observed (**Figure 4b**) under the same processing conditions. This throwback has caused a serious delay in the progress of the solar cells with PVD/CVD deposited perovskite.

Multiple trails were carried out to re-establish the PVD-CVD baseline, and to troubleshoot the reproducibility issue. The trail of extensive work led to a conclusion that the sublimated organic halide precursor decompose during the CVD process and accumulate in the walls of the CVD furnace, leading to severe reproducibility issues. A combination of pyrolytic and manual cleaning step (**Figure 4c**) has been adopted to clean the CVD tube to remove the decomposed residue. The cleaning procedure appears to be effective and results in faster and complete conversion of the PVD precursor into perovskite absorber as shown in **Figure 4d**.

Another major limitation for the process accuracy is the temperature control. The sublimation rate of the organic precursor FAI – and with that the conversion rate – is strongly dependent on the temperature. Small deviations of a few degrees already lead to a substantial change of the sublimation rate. The current set-up shows shortcomings in this respect and temperature deviations and overshoots can occur. External thermocouples allow to partially compensating for these effects. Still, the set-up needs to be re-designed and improved in the future.

Further re-optimization of process parameters are in place to re-establish the baseline. However, heating filaments integrated in our old tubular annealing set-up, resulting in undesirable thermal gradients, impose limitations on independent reliable control of the temperatures of substrate and sublimation source. Construction of a specifically designed reactor will be needed to prove the potential of PVD-CVD process – this would require significantly additional resources and time.

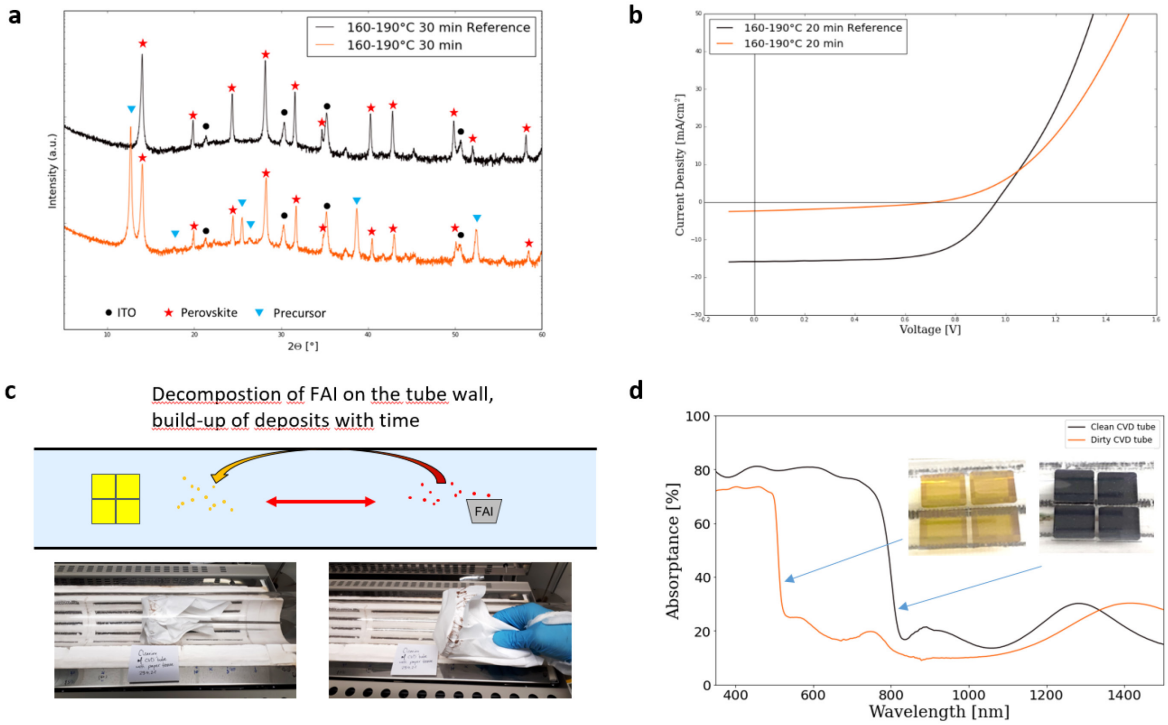

Figure 4. Reproducibility challenge with the CVD process. **a**, XRD pattern of perovskite layer using CVD process. The initial studies results are indicated with black curve and at a later month is indicated with orange. The presence of a high amount of residual precursor layer results in an incomplete conversion reaction. **b**, J-V curves of solar cells with identical layer stack and perovskite layers converted under the same CVD conditions. The reference device (black) reaches a PCE of 9.6%. The device processed some months later (orange) shows a much lower short circuit current and reduced open circuit voltage, reaching only 0.6% PCE. **c**, Residual decomposed FAI in the tube furnace retrieved from manual cleaning process. **d**, The difference in absorbance of perovskite layer before (orange) and after (black) cleaning procedure. For the same CVD conversion duration, the absorbance of perovskite layer is much lower in case of a dirty CVD tube compared to a strong absorbance spectra of perovskite after carrying out the cleaning procedure.

3.1.5 PVD+Blade coating as an alternative scalable method

To explore alternative hybrid method, we developed a **new** and **scalable** hybrid perovskite fabrication process, combining thermal evaporation and blade coating.[8] **Figure 5a** illustrates this novel fabrication process, which consists of three steps. In the first step, the inorganic halide template is sequentially deposited by thermal evaporation. This template consists of a 300 nm lead iodide (PbI_2) layer on top of a 15 nm cesium iodide (CsI) layer. In the second step, the organic halide precursor solution, composed of formamidinium iodide (FAI), methylammonium bromide (MABr), and methylammonium chloride (MACl) dissolved in isopropanol, is blade coated on the inorganic halide template at a substrate temperature of 65 °C and inducing the perovskite conversion with homogeneously distributed Cs. In the last step, thermal annealing at 150 °C for 15 min is performed in ambient air to promote crystal growth to reduce the grain boundaries and to obtain a compact perovskite film with large grain size.

This process has manifold advantages over non-hybrid perovskite fabrication process, such as the avoidance of toxic solvents for the inorganic halide precursors (1st step), the ready bandgap tuning by changing the perovskite composition (1st and 2nd step), the facile incorporation of passivation strategies and additives into the solution (2nd step), the conformal coating on rough substrates (1st step) and its ambient air processability (2nd step).

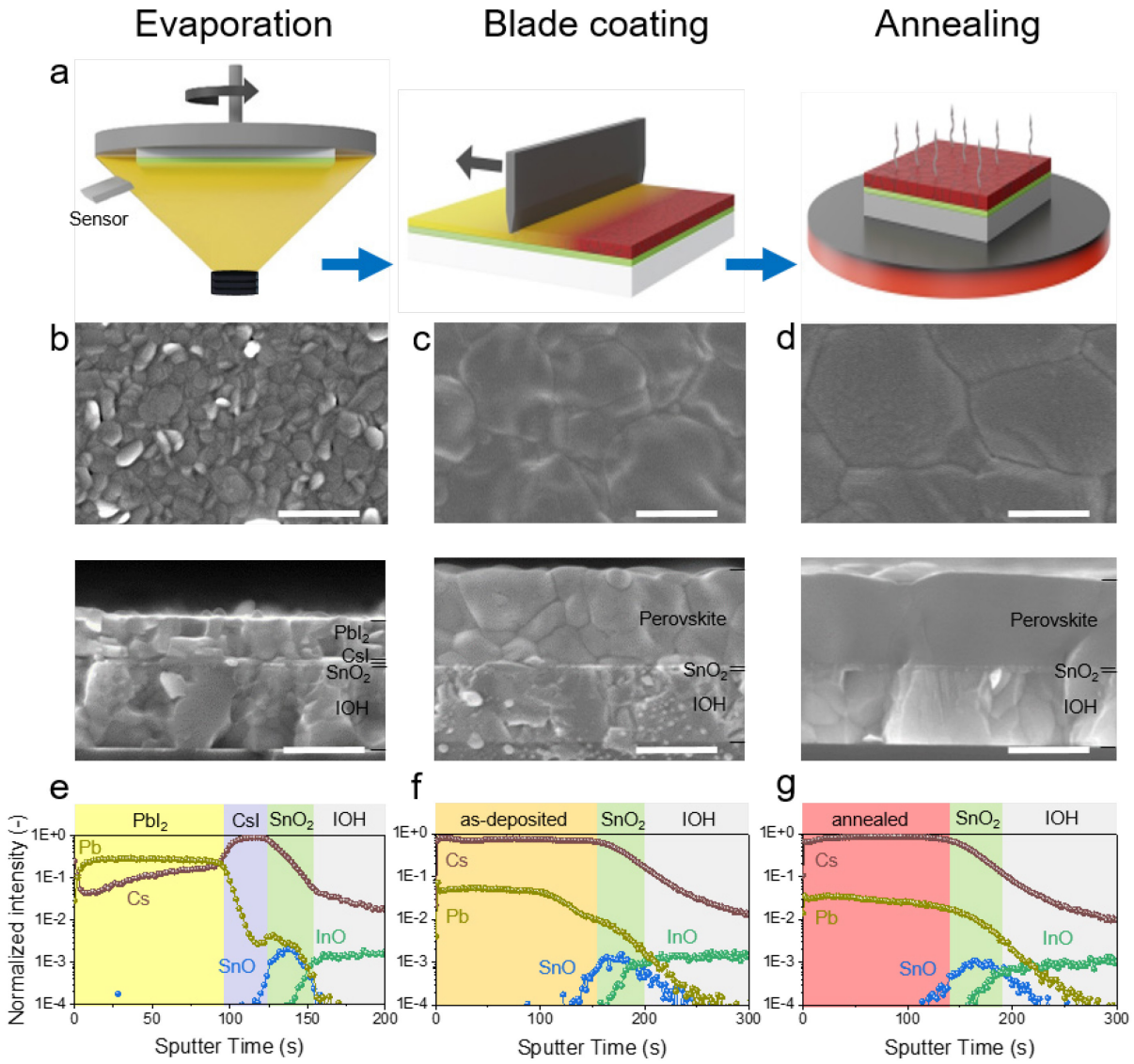

Figure 1: Hybrid PVD/blade coating process for perovskite films after each step. **a**, Schematic of the three steps of the PVD/blade coating fabrication process. SEM top/cross-section view images and ToF-SIMS depth profiles after each fabrication step: **b**, **e**) after evaporation, **c**, **f**) after blade coating and **d**, **g**) after thermal annealing. The scale bar is 500 nm.

We systematically investigated the influence of processing parameters on the perovskite formation mechanism during the PVD/blade coating process and elucidate the film growth mechanism. In **Figure 6**, we exemplarily provide the XRD and SEM data of solutions with different concentrations. For the low concentrated solution (30/3/3 mg/mL), only a fraction of the inorganic halide template reacted with the organic halides to perovskite in the upper region of the film. This perovskite capping layer inhibits the further diffusion of precursors and their reaction with the buried PbI_2. When the optimum concentration (60/6/6 mg/mL) was used, a compact perovskite film with minor PbI_2 was formed. For the highest concentration (90/9/9 mg/mL), rough and defective perovskite films with hexagonal perovskite δ-phase had which makes these films inappropriate for PV devices.

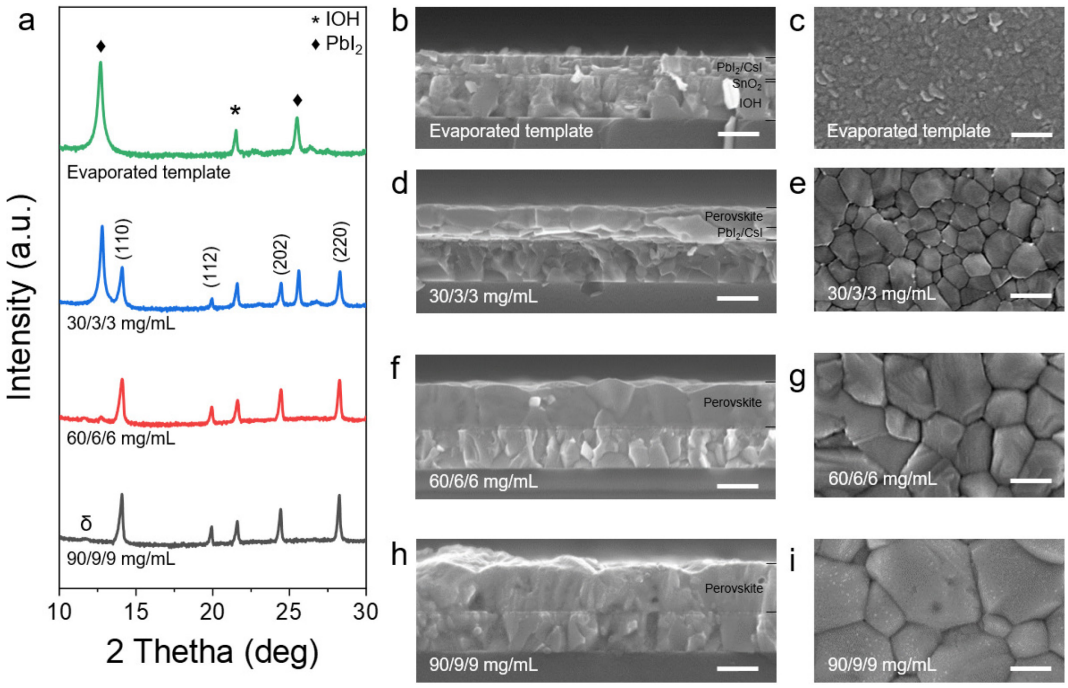

Figure 2: Evaporated inorganic halide template and perovskite films prepared by 30/3/3 mg/mL, 60/6/6 mg/mL and 90/9/9 mg/mL of FAI/MABr/MACl organic halide precursor solution concentration. **a**) XRD patterns (log-scale) with indicated diffraction peaks of the α-phase perovskite crystal planes. PbI_2 is labeled by ♦ and IOH by *. **b-i**) SEM cross-section and top view images of **b-c**) inorganic halide template and perovskite films prepared by different concentrations of the organic halide precursors: **d-e**) 30/3/3 mg/mL, **f-g**) 60/6/6 mg/mL and **h-i**) 90/9/9 mg/mL of FAI/MABr/MACl. The scale bar is 500 nm.

We reported a novel and scalable fabrication process of the perovskite film that combines the merits of the scalable solution- and vapor-based deposition methods, including facile compositional engineering to broadly tune the bandgap, and more importantly the avoidance of using toxic solvents. We systematically vary the processing conditions of the perovskite absorber to gain insights into the perovskite formation mechanism during the PVD/blade coating. Furthermore, this process can be adapted for wide bandgap perovskite films and be eventually applied to coat textured surfaces, e.g. in tandem solar cell applications. Ultimately, other meniscus-guided deposition methods can replace blade coating, such as slot-die coating or inkjet printing. Overall, the proposed method and its variants are easily scalable for large area manufacturing while the avoidance of toxic solvents is an additional advantage for successful commercialization of PSC technology. Besides, the processes can be applied on flexible foils as well, paving the way for roll-to-roll or sheet-to-sheet manufacturing in the future.

To obtain perovskite solar cells fabricated by scalable deposition methods and green solvents, we replaced the spin coating method for both charge transporting layers (SnO_2, Spiro-OMeTAD) by blade coating and replace the standard halogenated solvent (chlorobenzene) of the hole transporting material (Spiro-OMeTAD) by non-toxic p-Xylene solvent. In conjunction with the perovskite films fabricated by PVD/blade coating process, the optimized PSCs achieved high open-circuit voltage (V_{OC}) up to 1.16 V for a perovskite with an optical bandgap of 1.56 eV and a PCE up to 18.7 %, which is the highest reported efficiency of solution-based PSCs using green solvents only (**Figure 7**).

We demonstrated efficient PSCs fabricated by scalable deposition methods and without toxic solvents. These devices achieved excellent V_{OC} of 1.16 V and PCE up to 18.7 % with good uniformity on large-area substrates. With our work, we made an important contribution to reduce the performance gap between toxic and green solvent-based, scalable perovskite fabrication.

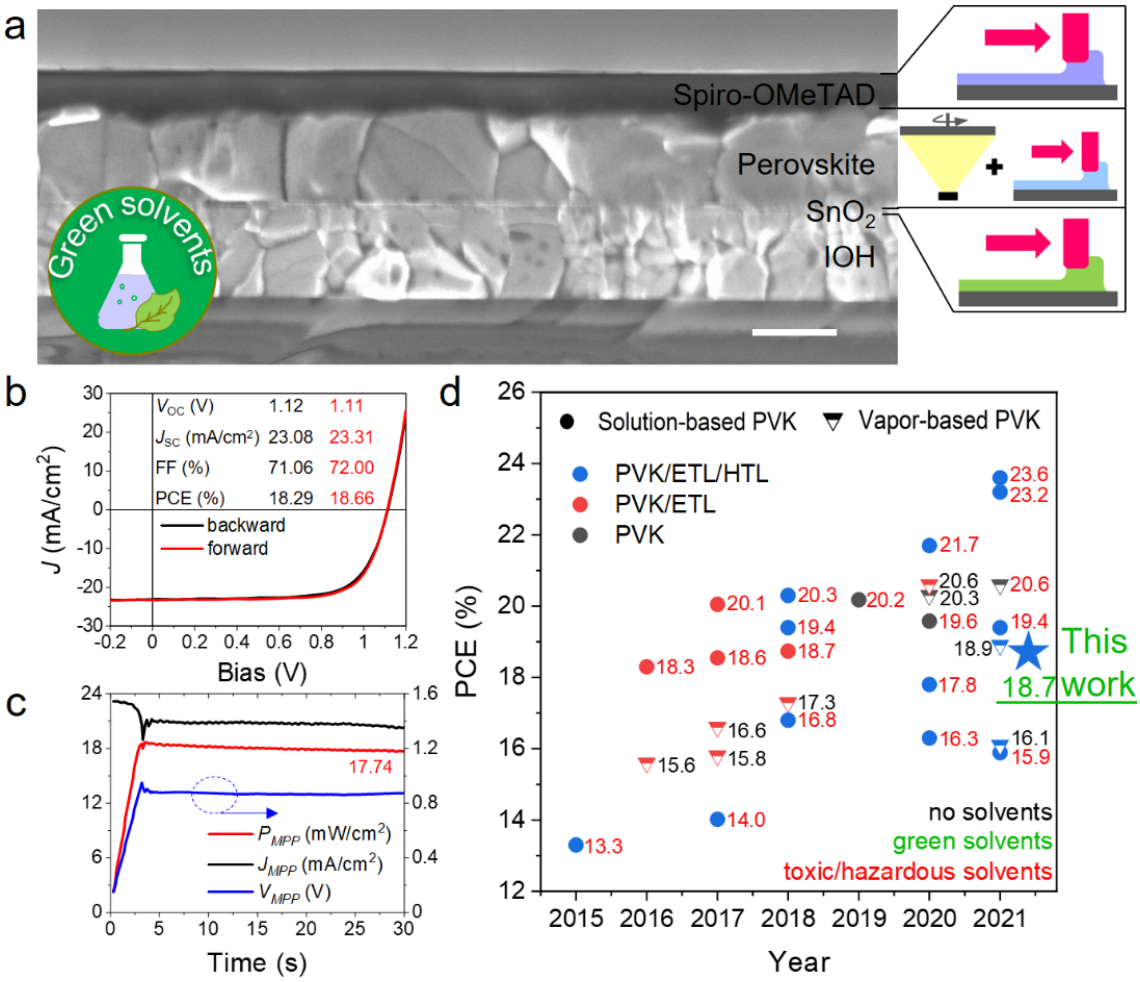

Figure 3. **a**, SEM cross-section view of PSC with blade coated charge transporting layers and perovskite layer by PVD/blade coating. The scale bar is 500 nm. **b**, Current-voltage characteristics and **c**, MPP tracking of the champion device with a cell area of 10 mm^2 on 50 mm x 50 mm substrates. **d**, Power conversion efficiency versus year for selected, small-area (~0.1 cm^2) devices with indicated layers fabricated by scalable deposition methods (symbol color). Additionally, devices are distinguished by solution- and vapor-based perovskite absorber layer (symbol type) as well as by the use of green or toxic/hazardous in the perovskite fabrication (font color). Perovskite (PVK), electron transporting layer (ETL) and hole transporting layer (HTL).

3.2 WP 2 - NIR transparent perovskite mini-module

3.2.1 Laser scribing on flexible substrate

We develop NIR-transparent perovskite mini-module on flexible substrate through a laser-based patterning approach to attain monolithic interconnection. As shown in the **Figure 8a**, the bottom electrode (IO:H electrode) is divided into individual subcells through P1 scribing. Then, the hole transport layer (HTL), perovskite absorber and electron transport layer (ETL) stacks are deposited subsequently. We utilize a hybrid deposition process utilizing a combination of physical vapor deposition (PVD) (for inorganic halide precursors) followed by spin-coating technique (organic halide solution) to coat the perovskite layer. After the deposition of the ETL stack, P2 scribing is carried out to create a pathway to connect the bottom and the top electrode of adjacent subcells. Finally, after the top electrode deposition, P3 scribing is carried out to isolate the top electrode from the two adjacent cells.

The flexible nature of the substrate and the limited conductivity of the transparent electrodes impose challenges to realize flexible NIR-transparent perovskite mini-module. The laser scribing process was carried out using 1064 nm pulse laser source. Scribing parameters such as pulse power, pulse frequency and scribing speeds were optimized for each scribing lines (**Table 1**). The confocal microscope image of the laser-based interconnections are shown in **Figure 8b**. The figure shows the selective removal of IOH with P1 scribing, HTL/perovskite/ETL with P2 scribing, and IZO/ETL/Perovskite/HTL with P3 scribing without inducing any damage to the flexible foil.

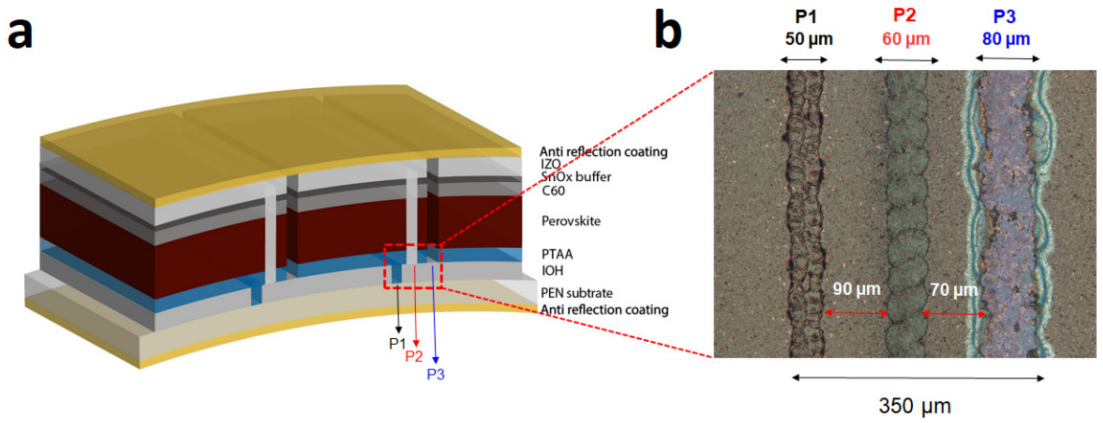

Figure 8. **a**, Schematic representation of NIR-transparent perovskite mini-module. **b,** Confocal microscopic image highlighting the laser-based P1, P2 and P3 interconnection in the flexible NIR-transparent mini-module. As shown, monolithic interconnections are realized through P1, P2 and P3 scribing and the width of the interconnection is around 350 µm.

Table 1: Laser scribing parameters for NIR-transparent perovskite mini-module on flexible substrates

Pattern	Power (mW)	Frequency (kHz)	Pulse period (µs)	Step size (µm)	Overlap (µm)	Repetitions
P1	900	20	100	9	20	1
P2	250	100	90	9	10	1
P3	125	20	60	3	10	1

3.2.2 All-laser scribing for NIR-transparent flexible perovskite mini-module

We adopt a judicious module layout to tackle the limited conductivity of the transparent electrode. The width of each subcell in the mini-module is limited to 5 mm, and the area utilized for interconnection is optimized to a narrow width of 350 µm to realize a high GFF (geometric fill factor) of 93%. Fiducial alignment markers were utilized to limit the safety width between the adjacent scribes to less than 100 µm. Adopting the optimized parameters, and through utilizing anti-reflection coating, we realized NIR-transparent perovskite mini-module with an efficiency of over 10.6% (**Figure 9a**) and an MPP efficiency of 10.5% (**Figure 9b**) with an active area of 2.25 cm^2. Further, the mini-module were fine-tuned to showcase excellent bifaciality, with a bifaciality factor of close to 95%. The mini-module performs at an efficiency of over 10% (MPP 10.01%) when illuminated through the top IZO electrode. At the moment, the relative difference in efficiency between the cell and mini-module is close to 5%, and can further be improved through process optimization.

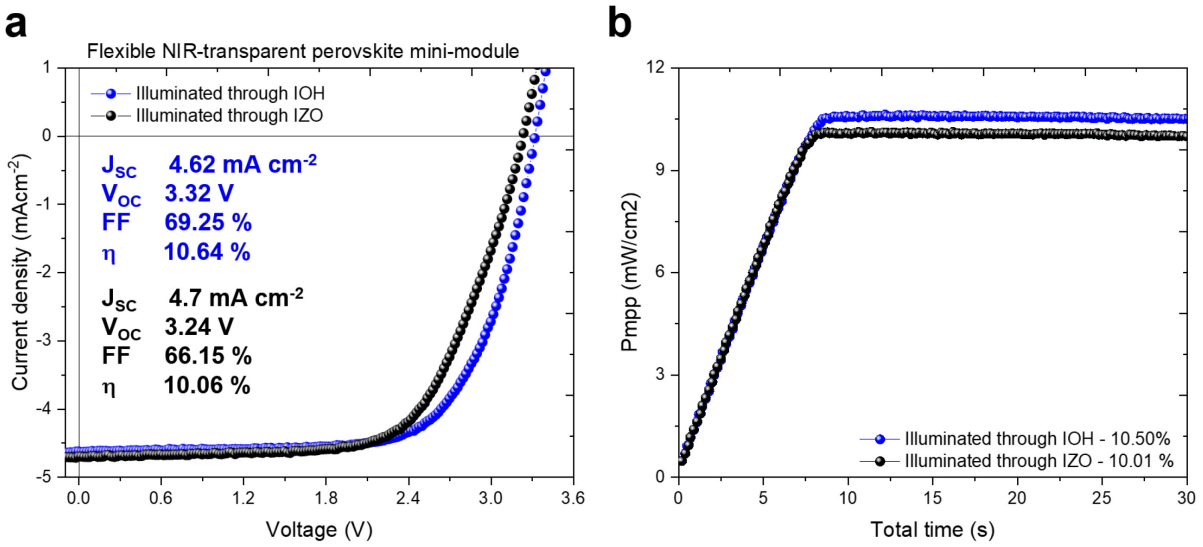

Figure 9. **a**, The J-V curve of NIR-transparent flexible perovskite mini-module illuminated from IOH and IZO side with corresponding PV parameters. **b**, MPP efficiency of NIR-transparent flexible perovskite mini-module.

3.3 WP 3: Investigation of performance stability of cells and modules

3.3.1 Accelerated life time tests of perovskite solar cells

As shown in **Figure 10a**, accelerated heat–light soaking (HLS) stability tests were performed on NIR-transparent solar cells until significant degradation could be observed. **Figure 10b** displays a cross-sectional scanning electron microscopy (SEM) image of the as-prepared perovskite solar cell investigated in this study. The cell was first tested under maximum power point (MPP) conditions for 1000 hours at 60 °C under continuous 1 sun illumination intensity in a 500 mbar N_2 atmosphere, and the cell still remained over 93% of its initial efficiency.[9] The cell was subjected to full area illumination, i.e., the cell edges, where the perovskite absorber is exposed to the environment, were also illuminated. Using the same device, illumination, and atmospheric conditions, the stress temperature was then increased to 80 °C to accelerate the degradation process. **Figure 10c** presents the normalized power output, V_{OC}, J_{SC}, and FF of a perovskite cell during 320 hours of MPP operation at 80 °C under continuous 1 sun illumination. As can be seen from **Figure 10c**, the catastrophic degradation regime is mainly dominated by a lower J_{SC} and a slightly decreased FF, while the V_{OC} even increased initially and then remained almost constant. The HLS experiment was stopped at around 320 h to avoid the complete

degradation of the device and enable further characterization to understand the underlying degradation mechanisms.

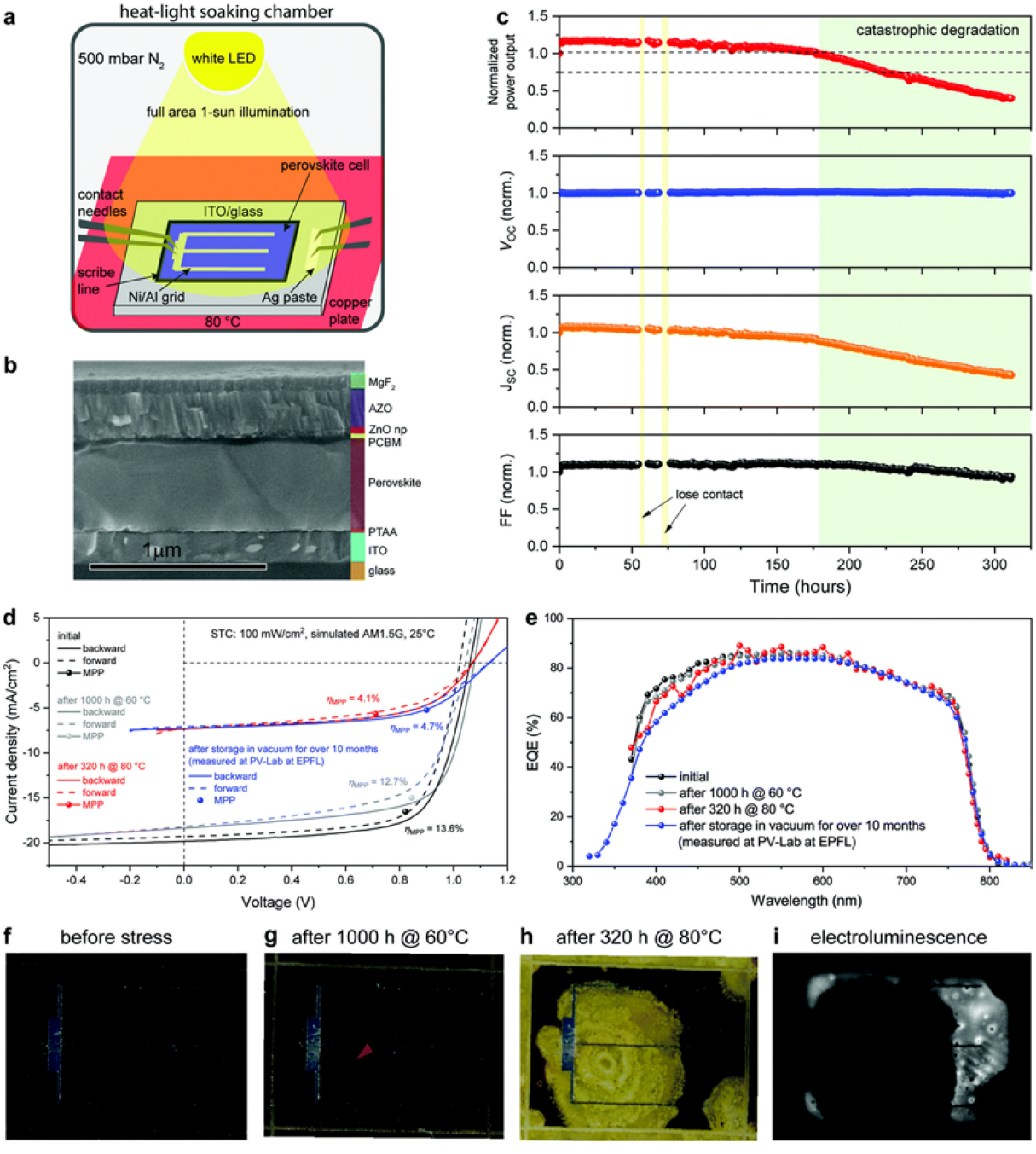

Figure 10. Operational stability under heat–light soaking (HLS). (**a**) Schematic illustration of the HLS experiments. A non-encapsulated NIR-transparent perovskite solar cell was kept at the maximum power point (MPP) under continuous 1 sun illumination intensity. The cell was placed on a copper plate heated to 80 °C and subjected to full-area illumination (scribe line included) under a 500 mbar N_2 atmosphere. (**b**) Cross-sectional SEM image of the perovskite solar cell before HLS. The device structure is glass/ITO/PTAA/perovskite/PCBM/ZnO nanoparticles/AZO/Ni–Al grid/MgF_2. (**c**) Normalized power output, V_{OC}, J_{SC}, and FF of the perovskite cell under HLS. (**d** and **e**) J–V curves (**d**) and EQE spectra (**e**) of the perovskite solar cell after different stress conditions. The J–V curves were measured under standard test conditions (STC: 100 mW cm^{-2}, AM 1.5G, 25 °C). (**f**–**h**) Photographs of the perovskite cell taken at different stages, i.e., before any HLS stress (**f**), after 1000 hours of HLS at 60 °C (**g**), and after 320 h of HLS at 80 °C (**h**). (**i**) Electroluminescence image of the cell after HLS at 80 °C for 320 h.

To accurately evaluate the dominant degradation losses, the photovoltaic performance of the perovskite device was measured immediately after HLS under standard test conditions (STC: 100 mW cm^{-2}, simulated AM 1.5G, 25 °C). As shown in **Figure 10d**, the cell started from a steady-state efficiency of 13.6%, which dropped to 12.7% after 1000 hours at 60 °C in N_2. After a further 320 hours of HLS at 80 °C, the cell delivered a stabilized efficiency of 4.1%, with this value increasing to 4.7% after 10 months of subsequent storage in a vacuum. **Figure 10e** compares the external quantum efficiency (EQE) measured before degradation, and after 1000 hours at 60 °C, 320 hours at 80 °C and vacuum storage for 10 months (the last two curves were acquired at the position of a remaining dark brown area of the cell). The EQE after degradation did not decrease significantly compared to before, which indicates that the measured J_{SC} loss mainly originates from the reduction of the cell active area as shown in the photographs (**Figure 10f–h**). Indeed, two distinct areas can be observed in **Figure 10h**: an inactive yellow area and an active dark brown area, as confirmed by electroluminescence imaging (**Figure 10i**). To verify that the decrease in J_{SC} indeed stems from the loss in the active area, the J_{SC} of the cell after 320 hours of HLS was re-calculated using only the brown region area. The re-calculated J_{SC} is close to the value calculated from the EQE, confirming our hypothesis.

Steady-state photoluminescence (PL) measured in the brown area shows a PL peak position of 781 nm (corresponding to an optical bandgap of 1.59 eV), which indicates that the bandgap of this region did not change throughout HLS at 60 °C and 80 °C. From **Figure 10f–h**, the inactive regions appear to originate from yellow spots that appeared during HLS at 60 °C (see e.g. the red arrow in **Figure 10g**) and then these domains grew outwards during HLS at 80 °C. Intriguingly, the majority of the cell edges did not act as degradation centers even though the perovskite is directly exposed to the N_2 atmosphere at the scribe lines.

3.3.2 Formulation of degradation mechanism

To gain further insights into the degradation mechanism, detailed morphological and chemical characterizations were performed. **Figure 11a** shows cross-sectional SEM images taken across the brown/yellow transition area of the full devices after 320 hours HLS at the MPP. Three distinct regions can be observed and are classified into a degraded area (left), a transition area (middle) and an intact area (right). Higher magnification SEM images (**Figure 11b–d**) show that the compact morphology with large grains of the absorber is maintained in the intact area (as in **Figure 11d**), while the degraded area (**Figure 11b**) exhibits a porous morphology indicative of a loss of material from the absorber. The transition area (**Figure 11c**) features voids of different sizes primarily within the absorber bulk instead of its interfaces. In that regard, the degradation mechanism of the perovskite cell investigated here at 80 °C in an N_2 atmosphere differs from previous reports: the perovskite bulk rather than the perovskite/charge transport layer interfaces seems to degrade first. The AZO layer appears broken and bent at certain positions in the degraded region away from the transition area (**Figure 11e**).

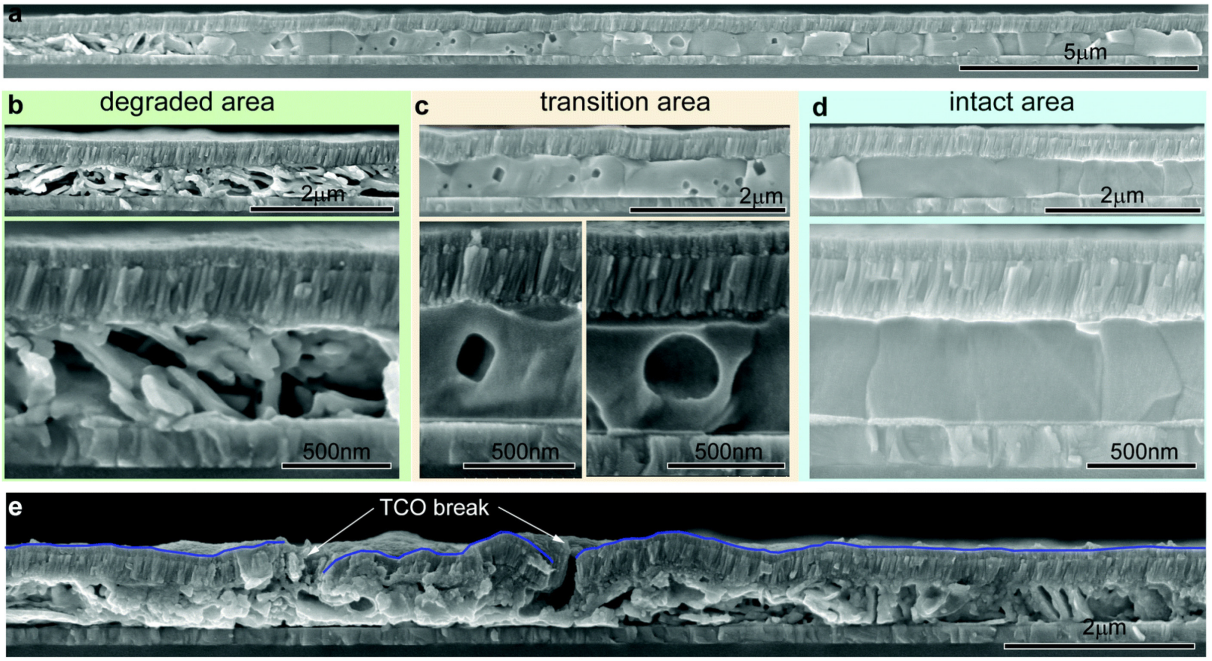

Figure 11. Microstructural analysis. (**a**) Low magnification cross-sectional SEM image spanning from the yellow to the brown areas of the perovskite cell after 320 hours HLS at 80 °C. Three different morphologies can be observed, which are assigned to the degraded area, transition area, and intact area. (**b**–**d**) High magnification cross-sectional SEM images of the degraded (**b**), transition (**c**), and intact areas (**d**). (**e**) Microstructure of a degraded area that features a broken top electrode.

Extracting a thin lamella of material using the conventional focused ion beam (FIB) method and performing a scanning transmission electron microscopy (STEM) energy-dispersive X-ray spectroscopy (EDX) analysis of one of the cracked regions (**Figure 12a–c**) reveals that Pb, I, and Br were expelled from the absorber and redeposited on the crack top surface (**Figure 12d**). This transport of material is indicative of pressure building up in the absorber, a pressure that eventually leads to a rupture of the top electrode. Regions richer in Pb suggestive of metallic Pb are marked by arrowheads at the crack edge. Other Pb-rich clusters are also observed (**Figure 12e**) inside the cell. These are surrounded by PbI_2 regions, in accordance with the XRD data (not shown here), and large voids, in line with the SEM data presented in **Figure 11d** (note that the fraction of voids is higher in the FIB-prepared cross-section due to preferential sputtering of perovskite regions not protected by other layers in the line of sight of the gallium ions). On the other hand, a FIB cross-section extracted from the non-degraded dark brown area exhibited a more compact microstructure and a distribution of elements as anticipated for a functional perovskite (**Figure 12f**, the presence of In and Mg within the absorber is an artefact of the quantification procedure). This preserved microstructure is in accordance with the SEM data shown in **Figure 10b** and **Figure 10d** and the EL data of **Figure 10i**.

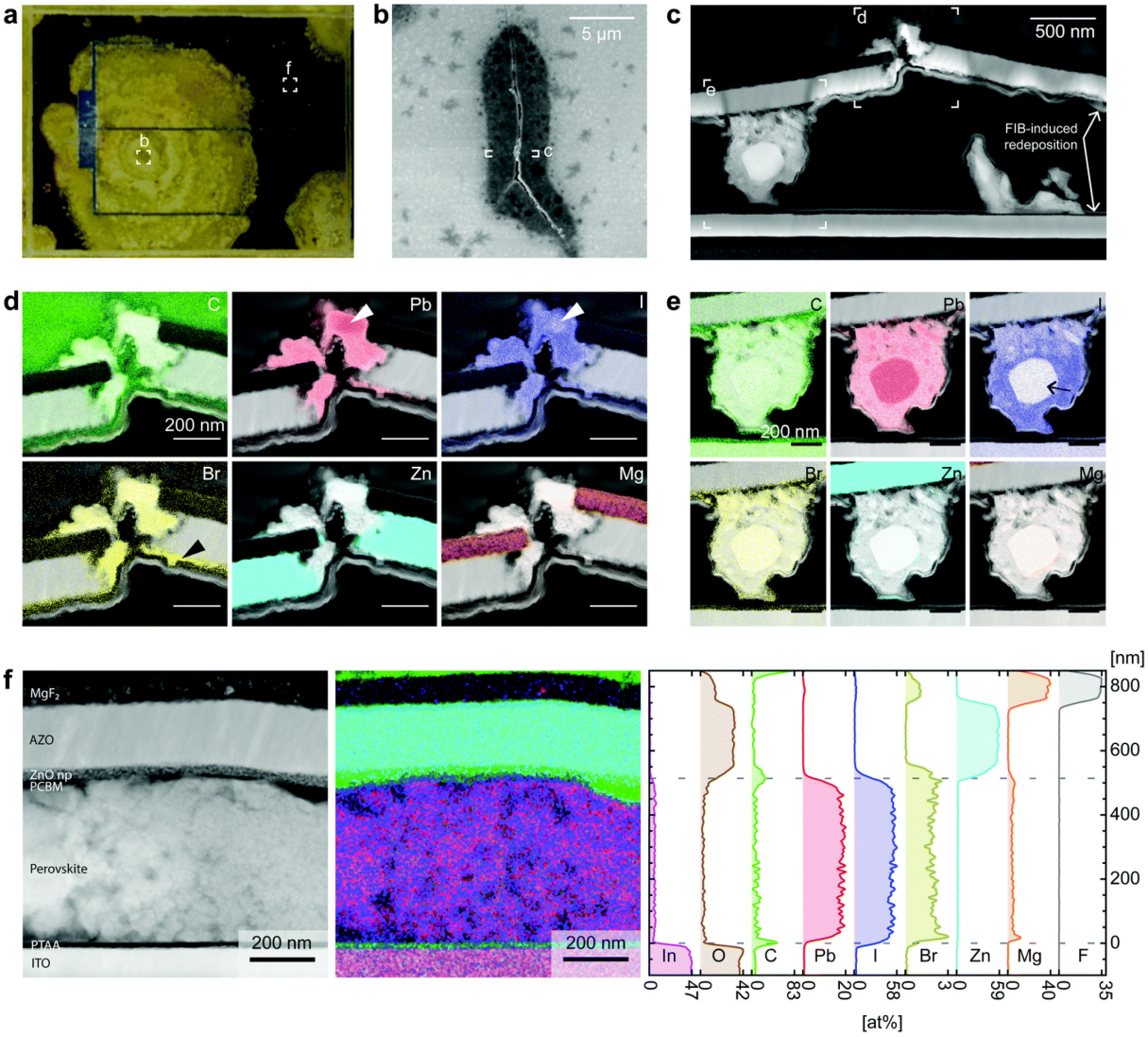

Figure 12. Chemical composition analysis. (**a**) Photograph of a perovskite cell after 320 h HLS indicating the region of interest for TEM characterization. (**b**) The top-view SEM image of a crack at the degradation nucleation seed. (**c**) STEM high-angle annular dark-field (HAADF) image of the cross-section of the area labeled in (**b**). (**d** and **e**) STEM EDX maps of the regions at the crack tip and within the cell, respectively. (**f**) STEM HAADF micrograph, STEM EDX map, and corresponding quantified line-scan of the cross-section of one dark brown area (area labeled **f** in (**a**)).

After comprehensive photovoltaic properties, phase composition, microstructural, and chemical composition analysis, we revealed an I_2 vapor induced degradation mechanism. As schematically shown in **Figure 13**, an I_2 vapor-triggered and -assisted degradation mechanism is proposed to account for the degradation behaviour under HLS. The degradation was observed to originate from a few seed points in the perovskite bulk rather than from the interfaces with the charge-selective layers or from the cell edges. I_2 vapor, first released at these defective points and then further released from the decomposition of the perovskite exposed to this vapor, controls the degradation process. Furthermore, this autocatalytic degradation process is shown to locally rupture the top electrode due to vapor pressure build-up. In addition to highlighting the detrimental influence of residual PbI_2, we show that such a degradation pathway can be alleviated by reducing the methylammonium and/or iodine content, providing a path to more stable perovskite solar cells. More details can be found in the publication.[10]

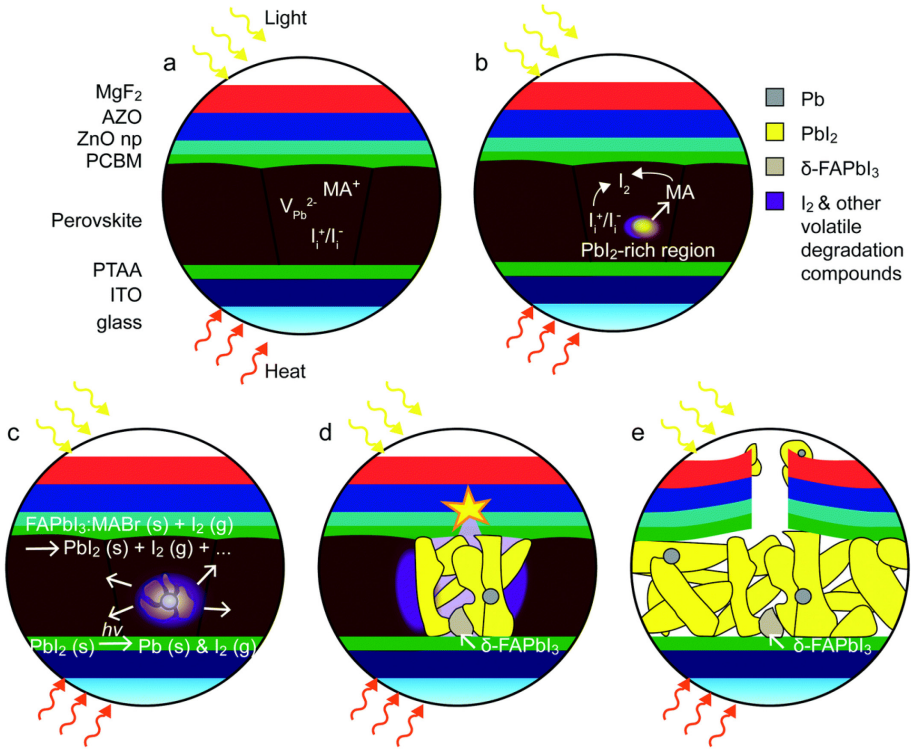

Figure 13. Schematic illustration of the I_2 vapor-assisted degradation mechanism. (**a**) Device structure of a starting perovskite solar cell. (**b**) PbI_2-rich regions and I_2 vapor start to appear after long-term HLS soaking in certain locations due to the loss of MA and/or I. (**c**) I_2 vapor triggers the degradation of the neighboring perovskite absorber to release more detrimental I_2 vapor; meanwhile, the degradation product PbI_2 could easily decompose into metallic Pb and release I_2 vapor, which accelerates the degradation process. (**d**) The perovskite decomposition process continues auto-catalytically, giving rise to a rise in pressure within the cell, with δ-$FAPbI_3$ forming locally due to the reaction of PbI_2 with the decomposition gases. (**e**) The top electrode eventually ruptures when the pressure is high enough to break the TCO.

3.4 WP 4 – Demonstration of 4 terminal tandem mini-module

To estimate the potential of the NIR-transparent flexible perovskite mini-module in a 4T tandem configuration, the perovskite mini-module is coated with an anti-reflection coating and is combined with a CIGS mini-module as depicted in **Figure 14a**. The ARC coating is applied onto the perovskite top cell to improve light coupling in the tandem stack. A monolithically interconnected CIGS mini-module consisting of 5 subcells with a standalone PCE of 15.4% is used as a bottom mini-module in this work.

The JV and EQE characteristic curves of the perovskite mini-module and CIGS bottom mini-module are displayed in **Figures 14b and 14c**. The performance of the standalone CIGS mini-module is also included in the plot for the sake of comparison. The corresponding PV parameters are tabulated in Table 2. The influence of the reduced light intensity can clearly be seen in the PV parameters of the CIGS bottom mini-module. The J_{SC} of the CIGS mini-module reduces from 6.6 mA cm^{-2} to 3.1 mA cm^{-2} owing to the absorption of the perovskite top module in the shorter wavelength. In the Figure 4c, the transmittance of the perovskite top module is super-imposed into the EQE plot to show the fraction of photons entering the bottom module. The difference between the transmittance of the perovskite mini-module and the EQE of the filtered CIGS bottom cell suggests reflection losses at the top and bottom mini-module interface. This can be mitigated in future works through better light management at the interface.

As a result of reduced light intensity, the CIGS mini-module performs at an efficiency close to 7.9% as a bottom module in the tandem configuration. In combination with the perovskite top mini-module, the flexible perovskite-CIGS mini module performs at an efficiency of 18.5% in the 4T tandem configuration. Consequently, the flexible tandem mini-module outperforms both the perovskite and CIGS standalone mini-module showcasing the effectiveness of this approach. To complement the JV performance, we also measured the steady state efficiency of the 4T tandem mini-module through an MPP tracker. The CIGS standalone system performs at a stabilized MPP efficiency of 15.40 %. In a tandem configuration, the combined efficiency of the top and bottom mini-module adds up to over 18%, resulting in a substantial improvement in the device performance compared to the standalone CIGS mini-module.

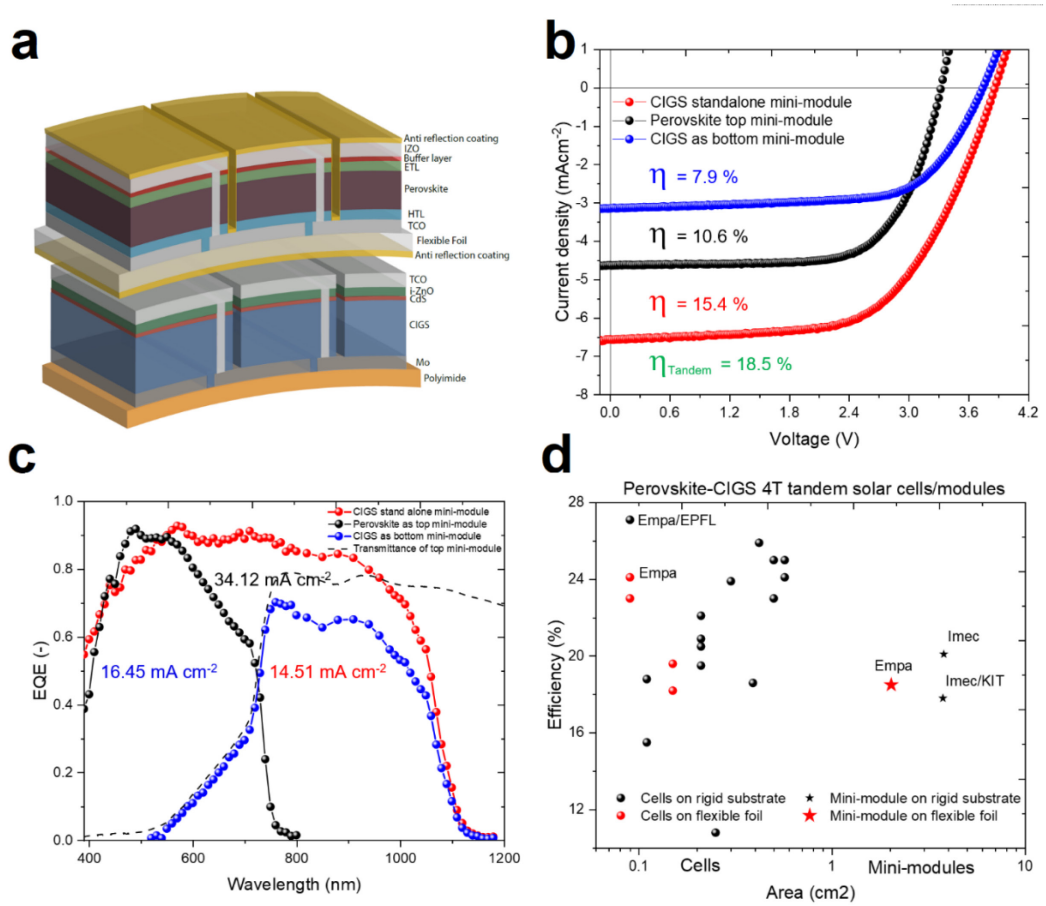

Figure 14: Photovoltaic performance of flexible perovskite-CIGS tandem mini-module. a) Schematic representation of flexible 4T tandem perovskite-CIGS mini-module. b) The JV and c) the EQE characteristics of NIR-transparent perovskite top mini-module (black), CIGS bottom mini-module (blue) in a 4T tandem configuration compared to the CIGS standalone mini-module (red). d) Reported efficiency of perovskite-CIGS tandem solar cells and mini-modules with their area. To account for variation in top and bottom subcell areas, the subcell with the smallest aperture area is considered.

As shown in **Figure 14d**, we demonstrate a proof of concept for flexible perovskite-CIGS tandem mini-module and have achieved efficiency comparable to the rigid counterpart. However, the perovskite absorbers were coated using laboratory scale PVD + spin-coating methodology. As a result, the 4T flexible perovskite-CIGS tandem mini-module were realized with an active area of just over 2 cm^2. To make this potent technology industrially favorable, in our future works, we would focus on developing high efficiency large-area wide-bandgap NIR-transparent perovskite mini-module on flexible substrate using fully scalable solution-based processing technique such as blade-coating or slot-die coating. For

the ease of industrial processing, special importance would be considered for the use of non-toxic green solvent system for solar cell processing. Further, engineering and design optimization on processing of NIR-transparent flexible perovskite mini-module would be adopted to push their GFF to over 95%.

Table 2: Photovoltaic parameters of the flexible perovskite-CIGS tandem mini-module.

Flexible mini-module	V_{OC} (V)	J_{SC} (mA/cm^2)	FF (%)	PCE (%)	Area (cm^2)
NIR-transparent perovskite mini-module	3.23	4.6	69.2	10.6	2.25
CIGS standalone mini-module	3.87	6.6	60.6	15.4	2.025
CIGS bottom mini-module	3.74	3.1	67	7.9	2.025
Tandem mini-module				**18.5**	

4 Conclusions & Outlook

This project has successfully demonstrated different scalable methods to deposit different individual layers of perovskite solar cells. The perovskite absorber was deposited both with a combination of PVD and CVD or PVD and Blade coating, resulting in homogeneous layers over 5cm x 5cm substrate size. Inorganic charge transport layers, such as NiO and SnO_2, and high mobility TCO, such as hydrogenated indium oxide (IOH), have been successfully developed using by magnetron sputtering and atomic layer deposition (ALD).

Despite a promising start, decomposition reactions and insufficient temperature control in CVD reactor have introduced several reproducibility problems and therefore significantly hindered the further development of the PVD-CVD process. Construction of a specifically designed reactor will be needed to prove the potential of PVD-CVD process. Alternatively, the PVD-Blade coating approach resulted in an impressive PCE over 18% after a short period of development. Using spin coated perovskite absorber, we achieved 17.5% NIR-transparent perovskite solar cells on flexible substrate, demonstrating the high efficiency potential of NIR-transparent solar cells directly grown on CIGS front-sheet, a foil used to encapsulate CIGS module.

Adopting accelerated stability tests on unencapsulated NIR-transparent perovskite solar cells, we revealed an I_2 vapor-assisted self-propagating degradation mechanism. At high operational temperature, the degradation initiates primarily from the perovskite absorber interior instead of the perovskite/charge-selective layer interfaces or cell edges. The release of I_2 vapor appears as the main degradation driver. After an initial release either from traces of PbI2 or from the perovskite itself, I_2 deteriorates the neighboring perovskite, releasing more I_2 and self-sustaining the degradation, which propagates across the active area. We show that the degradation pattern is independent of the perovskite composition and preparation method, charge selective layers, and top transparent contact, suggesting the universality of this I_2 vapor-assisted degradation mechanism in iodide containing halide perovskites. Overall, our results present new insights into the degradation mechanisms of perovskite solar cells operating under long-term light soaking conditions at high temperatures provide guidelines for further designing photo- and thermally-stable perovskite single junction and perovskite-based tandem photovoltaics.

To connect the individual cells into the monolithically connected module, we developed an all-laser scribing interconnection recipe on a flexible substrate. By optimizing the P1, P2, and P3 scribing lines, a high GFF of over 94% is achieved for the NIR-transparent mini-module on a flexible substrate. We demonstrate the first all-laser scribed NIR-transparent perovskite mini-module on a flexible substrate with an efficiency of 10.6%. Combining with a flexible CIGS mini-module, we demonstrate a proof-of-concept flexible perovskite-CIGS thin-film tandem mini-module with an efficiency of over 18%, on par with efficiency achieved on a rigid glass substrate.

Due to the severe reproducibility issue with the PVD-CVD method and limited access to the lab during the COVID-19 pandemic, the ambitious efficiency targets for NIR-transparent cell and mini-modules were not achieved. Encouragingly, the new PVD-Blade coating method developed as a backup method for PVD-CVD shows very high potential for upscaling the perovskite solar cells with high efficiency as promising cell efficiency (>18%) could be achieved just after a short period of development. Further work on the PVD-Blade coating method should focus on composition engineering and defect passivation to further reduce the V_{OC} of the cells to further improve the efficiency to a level comparable to solution-processed (such as blade coating or slot-die coating etc.) perovskite solar cells. In addition, further optimization is needed to coat perovskite film with high uniformity over a large area (10 cm x 10 cm) in view of mini-module fabrication. Regarding stability, strategies to further improve the device stability under operation conditions should be developed to ensure a lifetime comparable to existing PV technology, such as c-Si and CIGS. The investigation of the degradation pathway and associated degradation mechanism in the NIR-transparent perovskite mini-module are still scarce, which should be the focus of future studies.

To fully explore the low-cost potential of perovskite technology, in our future works, we would focus on developing high efficiency large-area wide-bandgap NIR-transparent perovskite mini-module on flexible substrate using fully scalable solution-based processing technique such as slot-die coating.

5 National and international cooperation

During the course of this project, we have close collaboration with EPFL (Prof. Ballif group) and CSEM on the sputtered NiO hole transport layer and ALD-SnO_2. In collaboration with Prof. Grätzel group from EPFL, we demonstrated over 27% perovskite-CIGS 4-terminal tandem solar cells, which is the current record for thin-film tandem solar cells.

6 Publications

The following work acknowledges the BFE funding:

1 C. Zhang, M. Chen, F. Fu, H. Zhu, T. Feurer, W. Tian, C. Zhu, K. Zhou, S. Jin, S. M. Zakeeruddin, A. N. Tiwari, N. P. Padture, M. Grätzel and Y. Shi, *Energy Environmental Science* 2022, DOI: 10.1039/D1EE04008A.

2 Severin Siegrist, Shih-Chi Yang, Evgeniia Gilshtein, Xiaoxiao Sun, Ayodhya N. Tiwari, Fan Fu, *J. Mater. Chem. A*, 2021, 9, 26680-26687.

3 T. Moser, K. Artuk, Y. Jiang, T. Feurer, E. Gilshtein, A. N. Tiwari and F. Fu, *J. Mater. Chem. A* 2020, 8, 21973-21982.

4 Y. Jiang, T. Feurer, R. Carron, G. T. Sevilla, T. Moser, S. Pisoni, R. Erni, M. D. Rossell, M. Ochoa, R. Hertwig, A. N. Tiwari and F. Fu, *ACS Nano* 2020, 14, 7502-7512.

5 Y. Jiang, S. Yang, Q. Jeangros, S. Pisoni, T. Moser, S. Buecheler, A. N. Tiwari and F. Fu, *Joule* 2020, 4, 1087-1103.

6 R. Kothandaraman, Y. Jiang, T. Feurer, A.N.Tiwari, F. Fu, *Small Methods* 2020, 4, 2000395.

7 F. Fu, S. Pisoni, Q. Jeangros, J. Sastre-Pellicer, M. Kawecki, A. Paracchino, T. Moser, J. Werner, C. Andres, L. Duchêne, P. Fiala, M. Rawlence, S. Nicolay, C. Ballif, A. N. Tiwari, S. Buecheler, *Energy Environmental Science* 2019, 12, 3074-3088.

7 References

1. J. Jeong et al., Pseudo-halide anion engineering for α-FAPbI3 perovskite solar cells. *Nature* 2021, 592, 381-385
2. S. Chen et al., Stabilizing perovskite-substrate interfaces for high-performance perovskite modules. *Science* 2021, 373, 902-907
3. H. Eggers et al., Inkjet-Printed Micrometer-Thick Perovskite Solar Cells with Large Columnar Grains. *Adv. Energy Mater*. 2020, 10, 1903184
4. L. Qiu et al., Hybrid chemical vapor deposition enables scalable and stable Cs-FA mixed cation perovskite solar modules with a designated area of 91.8 cm2 approaching 10% efficiency. *J. Mater. Chem. A*, 2019, 7, 6920-6929
5. J. Li et al., Highly Efficient Thermally Co-evaporated Perovskite Solar Cells and Mini-modules. *Joule* 2020, 4, 1035-1053
6. R. Swartwout et al., Scalable Deposition Methods for Large-area Production of Perovskite Thin Films. *Energy Environ. Mater*. 2019, 2, 119-145
7. T. Moser et al., Revealing the perovskite formation kinetics during chemical vapour deposition. *J. Mater. Chem. A* 2020, 8, 21973-21982
8. S. Siegrist et al., Triple-cation perovskite solar cells fabricated by a hybrid PVD/blade coating process using green solvents. *J. Mater. Chem. A* 2021, 9, 26680-26687
9. F. Fu et al., Compositionally Graded Absorber for Efficient and Stable Near‐Infrared‐Transparent Perovskite Solar Cells. *Adv. Sci.* 2018, 5, 1700675
10. F. Fu et al., I_2 vapor-induced degradation of formamidinium lead iodide based perovskite solar cells under heat–light soaking conditions. *Energy Environ. Sci.* 2019, 12, 3074-3088